journal

J. Am. Ceram. Soc., 94 [10] 3494–3499 (2011)
DOI: 10.1111/j.1551-2916.2011.04649.x

Ab Initio Computations of Electronic, Mechanical, and Thermal Properties of ZrB_2 and HfB_2

John W. Lawson,[‡,†] Charles W. Bauschlicher Jr.,[§] and Murray S. Daw[¶]

[‡]Thermal Protection Materials Branch, NASA Ames Research Center, Mail Stop 234-1, Moffett Field, California, 94035

[§]Entry Systems and Technology Division, NASA Ames Research Center, Mail Stop 230-3, Moffett Field, California, 94035

[¶]Department of Physics and Astronomy, Clemson University, Clemson, South Carolina, 29631

A comprehensive *ab initio* analysis of the ultra high temperature ceramics ZrB_2 and HfB_2 is presented. Density functional theory (DFT) computations were performed for the electronic, mechanical, thermal, and point defect properties of these materials. Lattice constants and elastic constants were determined. Computations of the electronic density of states, band structure, electron localization function, etc. show the diverse bonding types that exist in these materials. They also suggest the connection between the electronic structure and the superior mechanical properties. Lattice dynamical effects were considered, including phonon dispersions, vibrational densities of states, and specific heat curves. Point defect (vacancies and antisites) structures and energetics are also presented.

I. Introduction

The materials often referred to as ultra-high temperature ceramics (UHTC) are characterized by high melting point, high strength, and good chemical stability. The relatively good oxidation resistance of the diboride class of materials, in particular ZrB_2 and HfB_2, has attracted special attention, both as pure materials and as constituents in composites.[1,2,3,4] They are candidates for applications which require high temperature materials that can operate above 3000 K with little or no oxidation. These include the extreme environments experienced during hypersonic flight, atmospheric re-entry, and rocket propulsion. Aerospace applications include sharp leading edges and nose caps for hypersonic reentry vehicles. Sharp leading edges will enable greater maneuverability and cross range during reentry. The high temperatures generated at sharp leading edges, however, will require new materials with properties beyond the current state of the art.

Despite the thermal and chemical stability of UHTCs, many scientific challenges related to processing, characterization, and performance under operating conditions remain. As a result, these materials are not currently widely used. Basic research is needed to understand microstructural evolution, property improvement, and response to high temperature reactive environments seen in atmospheric reentry. The refractory nature of these materials means they must be processed at high temperature and pressure, although efforts to use pressureless sintering is ongoing.[5] Oxidation resistance has been improved through the use of additives; however, it remains an issue especially in high temperature reactive environments. These materials also display low fracture toughness which must be addressed as well.

Many of these challenges could benefit from computational modeling. In this article, *ab initio* modeling of the UHTC materials ZrB_2 and HfB_2 is performed. *Ab initio*, first principles methods are the most accurate modeling approaches available and represent a parameter free description of the material based on the quantum mechanical equations. In particular, we employed density functional theory (DFT) where the fundamental quantity is the electron density. In general, *ab initio* approaches can be computationally demanding. However, for single crystals with relatively small unit cells, the high symmetry of these systems can make a full *ab initio* treatment tractable. Using these methods, we obtained many of the intrinsic properties of these materials. In this article, we present results on structural quantities (lattice constants, bond lengths, etc.), electronic structure (bonding motifs, densities of states, band structure, etc.), thermal quantities (phonon spectra, phonon densities of states, specific heat), as well as information about point defects such as vacancy and antisite formation energies.

II. Method

All calculations were performed using DFT as developed by Perdew, Burke, and Ernzerhof (PBE).[6] These methods give very good results for calculations on solids. We used the plane wave DFT codes VASP[7,8,9] and ABINIT.[10,11] These codes have significant overlap, but also have a number of distinct features. Using different codes with differing methodologies also allows us to cross-check our results. With VASP, the projected augmented wave (PAW) potentials were used while with ABINIT, Fritz Haber Institute (FHI) pseudopotentials which are of the Troulliers–Martin form (Tr–Ma)[12] were employed. In general, the PAW potentials are expected to be slightly more accurate, and computationally more efficient, than those of Tr–Ma. However, in our computations, we found largely similar results. All quantities were converged individually with respect to k-point sampling and the plane wave energy cutoff. Dense k-point meshes were typically used, sometimes up to $40 \times 40 \times 40$ grids, along with a plane wave cutoff energy of 400 eV. The method of Methfessel and Paxon was used with a smearing parameter of 0.1 eV.

III. Atomic Structure

The materials, ZrB_2, and HfB_2, are an interesting mix of atomic species. Boron, which these two materials have in common, is a relatively small atom with an atomic radius of 0.9 Å and an atomic weight of 10.8 g/mol. Boron's electronic configuration is $[He]2s^2 2p^1$, giving it one less valence electron than Carbon. This electron "deficiency" has a significant impact on the properties of pure Boron whose ground state

W.-Y. Ching—contributing editor

Manuscript No. 29044. Received December 28, 2010; approved April 23, 2011.
[†]Author to whom correspondence should be addressed. e-mail: john.w.lawson@nasa.gov

structure is still unresolved. In pure materials, Boron is known to form strong covalent bonds.

Zirconium and Hafnium, on the other hand, are relatively large transition metal (TM) atoms. Zirconium has an atomic radius of 1.6 Å and an atomic weight of 91.2 g/mol while Hafnium has an atomic radius of 1.59 Å and an atomic weight of 178 g/mol. The electronic configuration for these elements is very similar: $[Kr]4d^2 5s^2$ for Zr and $[Xe]4f^{14}5d^2 6s^2$ for Hf. Thus, both species have two "*s*" and two "*d*" valence electrons to donate to the electronic structure of the material. Because of the very similar electronic configurations and atomic radii of Zr and Hf, we expect ZrB_2 and HfB_2 to have very similar bonding motifs and electronic structure. At the atomic level, the principal difference between Zr and Hf is their atomic weights. This difference will show up most prominently in the vibrational properties.

The crystal structure of both ZrB_2 and HfB_2 is the AlB_2-type TM diboride designated as C32 with space group symmetry *P*6/*mmm*. The structure is shown in Fig. 1. These materials are layered with alternating planes of pure TM and pure B. In the TM planes, the atoms have a closed packed hexagonal structure where each atom has six neighbors. The Boron planes have a graphitic structure with six membered rings and a coordination number of three. The TM and B planes are situated such that the TM atoms lie above (and below) the center of Boron rings in the neighboring planes. Thus, each metal atom has 12 Boron atoms as the nearest neighbors. The primitive cell of these structures contains one formula unit (one TM and two Borons) and the crystal has simple hexagonal symmetry (D_{6h}). Primitive vectors can be chosen to position the metal at (0,0,0) and the two Borons at (1/3,2/3,1/2) and (2/3,1/3,1/2) inside the unit cell. Thus, the hexagonal lattice constant "*a*" gives the metal–metal atom distance within a plane and the "*c*" lattice constants give the metal–metal atom distance in alternate planes. The reciprocal space Brillouin zone is also hexagonal.

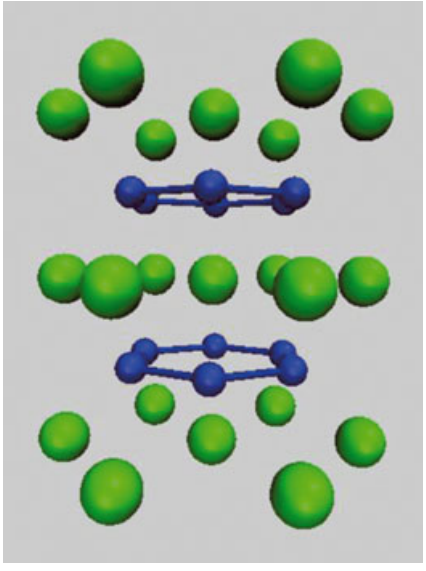

Fig. 1. Layered *C*32 diboride lattice structure. Boron atoms (blue) have open hexagonal structure. Zr/Hf atoms (green) are HCP. Metal atoms are centered above and below six membered Boron rings.

The first step in our computations is the determination of the lattice constants. This is accomplished in a straightforward way by minimizing the total energy with respect to these parameters. These constants are largely determined by bonding and the atomic sizes. Our results are presented in Table I. As expected, ZrB_2 and HfB_2 have very similar lattice constants. Agreement with experiment is excellent. With the optimized lattice structure, we obtain the cohesive energy E_c of the optimized structure by subtracting the total energy of the crystal from the sum of the total energies of the isolated atomic constituents. These numbers are also given in Table I. Uncorrected atomic energies from the FHI potentials are known to be unreliable.[12] We therefore obtained them using results from reference materials for pure Zr, Hf, and B.

Detailed bonding information can be obtained from the electron localization function (ELF).[13,14] The ELF measures the probability of finding an electron near a reference electron located at a given point and with the same spin. Physically, this measures the spatial localization of the reference electron and thus provides information about the electron pair distribution. As such, it is useful for identifying covalent bonds. This is in constrast to the electron density which gives the single particle distribution only. For ZrB_2 in Fig. 2, we show slices of the full, three dimensional ELF. The first pane shows the ELF in the plane of the Zirconium atoms; the second pane shows the Boron plane; and the third pane shows a diagonal slice through a Zr atom and four of it neighboring B atoms. Atoms are shown as black, filled circles. Darker color indicates higher ELF where the ELF is constrained to give values between [0,1]. All three cuts show strong localization near the atomic cores. Away from the core, however, the Zr plane (left pane in Fig. 2) shows a diffuse structure with little localization between atoms. This behavior is typical of metallic bonding. Interestingly, however, triangular accumulation regions are seen between groups of three Zr. In the Boron planes (middle pane of Fig. 2), on the other hand, strong localization is evident between the atoms which is indicative of highly directional, covalent bonding. Similar results are expected for HfB_2.

An open question, however, is the nature of the bonding between layers. The expectation is that since Boron is considered electron deficient, it readily accepts charge from the Zirconium. The ELF slice across the planes and between the Zr-B atoms (right pane of Fig. 2) gives no indication of localization between the atoms. In fact, a zone with little or no ELF exists between the Zr and B, suggesting little or no covalent bonding between the layers. Thus, it is likely that the bonding character between layers is ionic.

To get a better idea about possible ionic bonding, we calculated the amount of charge transfer between the atomic

Table I. Structural and Mechanical Constants. Quantities in Parenthesis are Unrelaxed. Units are Å, eV/cell, and GPa. Experimental Results are from Reference 2 and 19

	a	*c*	E_c	C_{11}	C_{12}	C_{13}	C_{33}	C_{44}	*B*	*G*	*A*
ZrB_2											
PBE–Tr–Ma	3.17	3.55	21.41	553(556)	60(57)	113	419	234	233	226	0.75
PBE–PAW	3.17	3.56	22.23	563(565)	64(62)	133	446	253	248	234	0.79
Exp.	3.17	3.53		568	57	120	436	247	240	234	0.77
HfB_2											
PBE–Tr–Ma	3.15	3.52	22.07	578(579)	71(69)	118	430	238	244	231	0.74
PBE–PAW	3.14	3.50	22.47	609	73	135	470	266	263	249	0.77
Exp.	3.14	3.48									

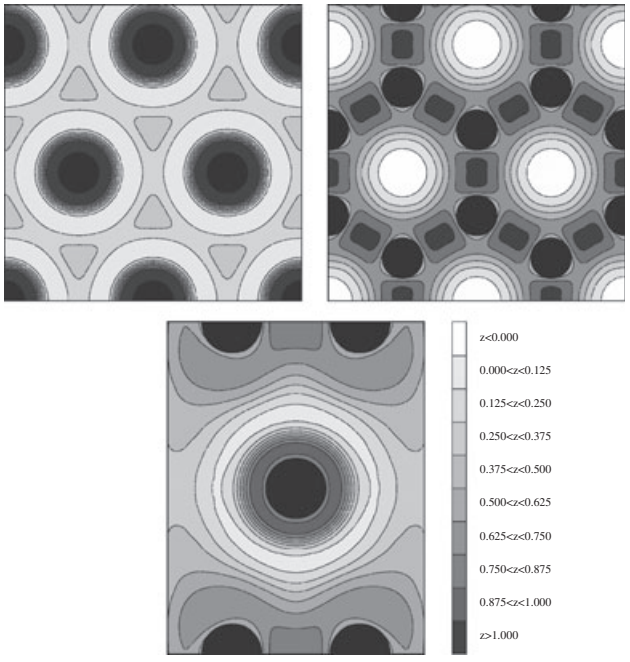

Fig. 2. Electron localization function (ELF) in a Zr plane (upper left), a B plane (upper right) and a cut-diagonal Zr-B plane (lower). The central atom in the lower panel is a Zr atom. ELF plots indicate metallic, covalent, and ionic-bonding motifs, respectively, are present in these materials.

layers. In a plane wave basis, however, this is nontrivial, since the basis functions span the entire cell and are not localized around individual atoms as with molecular, Gaussian basis sets. One possibility is to project the electronic states onto atom-centered spherical functions and then extract the electronic populations. However, this requires defining a Reitz–Wigner radius which is difficult to do consistently in a binary system with very different atomic radii. A better method is to calculate the Bader charges.[15] In this approach, space is divided into atomic regions where the dividing surfaces are minima of the charge density. By integrating the electron density inside these regions, the local electron charge is obtained. We performed this type of analysis and found significant charge transfer from Zr to B. The results are given in Table II. A single unit cell of ZrB_2 or HfB_2 will have one metal atom (with four valence electrons) and two Borons atoms (with three electrons each). We see that for ZrB_2, the Zr atom loses 1.43 electrons which is split between the two Borons. Similarly, for HfB_2, the Hf atom loses 1.44 electrons. This large charge transfer results in ionic bonding between the layers.

IV. Electronic Structure

We next examine the electronic structure of these materials. The density of states (DOS) is a compact representation of the electronic structure and gives the number of states in a small interval near a given energy E. The DOS for both ZrB_2 and HfB_2 are presented in Fig. 3 and have similar structure. First, a low energy peak appears near −10 eV and this is due to localized, tightly bound s electrons of Boron. These states are not expected to play a significant role in the bonding. Second, bonding states of Zr/Hf -d and B-2p are responsible for the large peak near −4 eV. These states are degenerate in energy and therefore could indicate the possibility of covalent bonding between the metal atoms and Boron. However, the low ELF values as well as the significant charge transfer between layers argues for ionic rather than covalent bonding. Finally, above the Fermi level are antibonding states.

An important feature of the DOS is the existence of a pseudogap: a sharp valley around the Fermi level. A finite DOS at the Fermi level indicates some metallic behavior resulting mainly from metallic bonding between Zr/Hf (d orbitals at E_F). This metallic behavior is responsible in part for the high thermal conductivity in these materials. On the other hand, the separation of full, bonding states, and empty antibonding states gives these materials many of the favorable cohesive properties often seen in insulators, such as high melting point and chemical stability. In fact, in other diborides, for example TaB_2 or NbB_2, the Fermi level is shifted out of this valley, resulting in a deterioration of properties.[16] These results are consistent with X-ray photoelectron spectra and NMR results.[17,18]

A more detailed representation of the electronic states can be obtained from the band structure. In our calculations, there are 10 valence electrons, and therefore, five occupied bands per k-point. The band diagram for ZrB_2 is shown in

Table II. Bader Charges Per Atom Give the Amount of Charge Transfer Between the TM and Boron Atomic Layers. A Unit Cell Has 10 Electrons with One Zr/Hf (Z = 4) Atom and Two B (Z = 3) Atoms. The Large Charge Transfer Indicates the Interlayer Bonding Is Ionic

	TM atom	B atom
ZrB_2	2.57	3.72
HfB_2	2.56	3.72

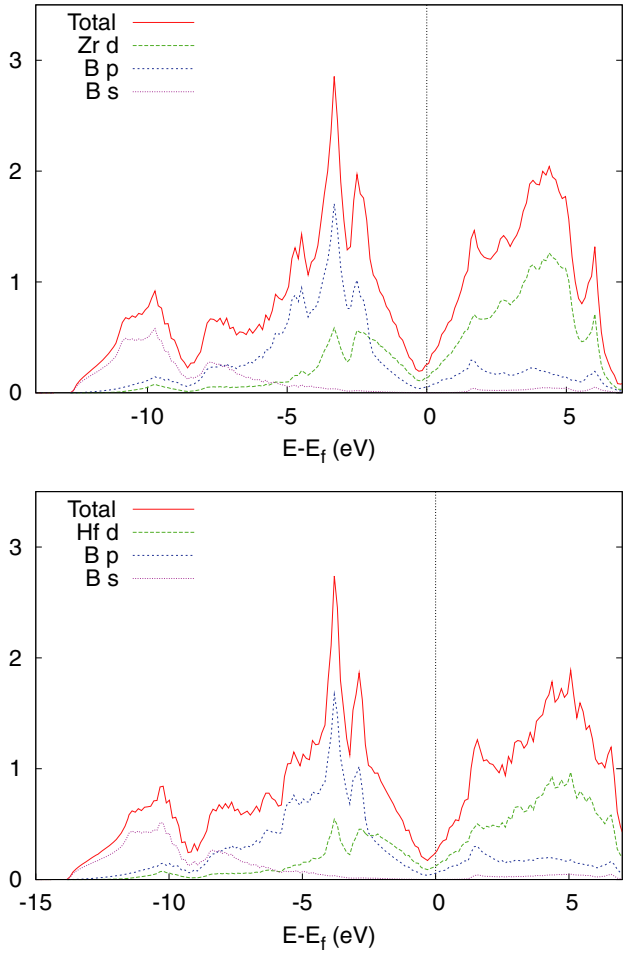

Fig. 3. Calculated total and site projected density of states for ZrB_2 (top) and HfB_2 (lower). The materials are electronically very similar owing to comparable atomic radii and valence for Zr and Hf.

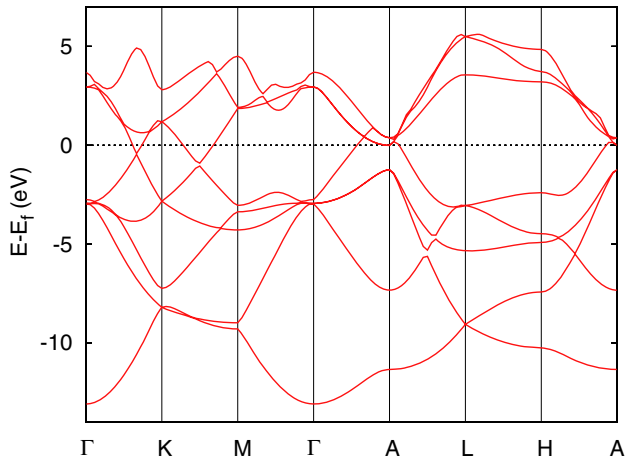

Fig. 4. ZrB_2 band structure along high symmetry directions in reciprocal space. Results for HfB_2 are largely similar.

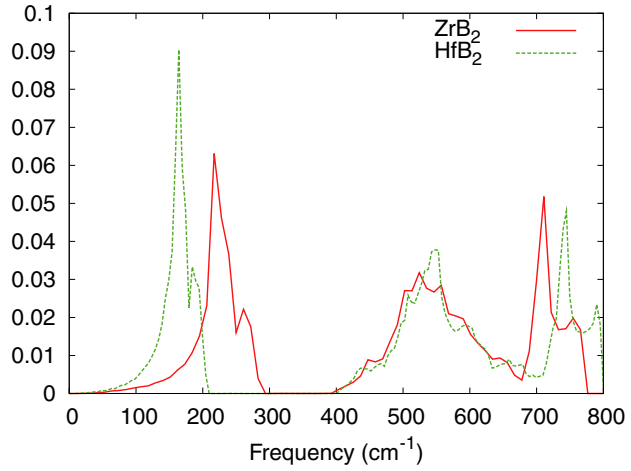

Fig. 5. ZrB_2 (solid/red) and HfB_2 (dashed/green) phonon density of states. HfB_2 has a larger phonon gap between acoustic and optical modes compared to ZrB_2 due to the Zr/Hf mass difference.

Fig. 4. Similar results can be obtained for HfB_2. The lowest band represents the Boron s states as seen in the DOS. Higher bands correspond to metal d and Boron p states.

V. Elastic Properties

Next, the elastic constants of these materials were calculated. This was done in two ways. First, results were obtained from density functional perturbation theory (DFPT) as implemented in ABINIT.[22] Second, they were calculated using the finite difference (FD) method implemented in VASP. In general, DPPT is expected to be more accurate than FD due to the lack of finite step numerical error. However, we find largely similar results with both methods.

For materials with $C32$ symmetry, the five independent constants were taken to be (C_{11}, C_{12}, C_{13}, C_{33}, C_{44}). From these, we evaluated the bulk modulus

$$B = \frac{2}{9}(C_{11} + C_{12} + 2C_{13} + \frac{1}{2}C_{33}), \quad (1)$$

the shear modulus

$$G = \frac{1}{30}(C_{11} + C_{12} + 2C_{33} - 4C_{13} + 12C_{55} + 12C_{66}) \quad (2)$$

and the anisotropy ratio

$$A = C_{33}/C_{11}. \quad (3)$$

Experimental results for the elastic constants are available for single crystal ZrB_2,[19] however, they are not available for HfB_2. Our computed values agree very well with experimental numbers for ZrB_2 and with previous theoretical results.[20,21] This suggests that the values we obtained for HfB_2 are also reliable. Computed elastic constants are slightly higher for HfB_2 than for ZrB_2 which is consistent with the shorter bond lengths. Relaxation effects were also evaluated and found to be negligible.

VI. Vibrational and Thermal Properties

Next, we considered lattice dynamical properties for ZrB_2 and HfB_2. These are relevant for thermal and transport properties as well as interaction with radiation such an infrared (IR) and Raman scattering. As with the elastic constants, lattice dynamics was computed in two ways. First, with ABINIT, DFPT calculations were performed.[23] Second, with VASP, the supercell method with finite differences was used. In each case, the dynamical matrix was constructed on a $6 \times 6 \times 6$ k-space mesh. The phonon densities of states (pDOS) for ZrB_2 and HfB_2 are shown in Fig. 5. As can be seen, the pDOS for both materials split into a low frequency and a high frequency region which are separated by a finite gap. By plotting the partial pDOS (not shown), the low frequency, acoustic modes can be related primarily to Zr/Hf atom vibrations whereas the high frequency, optical modes are either pure Boron states or mixed TM-Boron modes. Interestingly, the Boron modes are very similar for the two materials whereas the Zr and Hf components are shifted relative to each other. This shift is easily explained by the mass difference between Zr and Hf. Thus, interestingly, while the electronic DOS for ZrB_2 and HfB_2 were almost identical due to their similar valence structure and atomic radii, the pDOS have a noticeable difference due to the atomic mass difference.

Phonon dispersion curves are plotted in Fig. 6. The unit cells of ZrB_2 and HfB_2 contain three atoms which give a total of nine phonon branches: three acoustic and six optical branches. As mentioned, the acoustic modes result from Zr/Hf motion, whereas the upper optical modes are mainly from motion of the much lighter Boron atoms. Acoustic branches have steep slopes near $\vec{\mathbf{k}} = \Gamma$ consistent with large elastic constants. However, they show considerably less dispersion in the z direction. Numerical values for the modes at $\vec{\mathbf{k}} = \Gamma$ are given in Table III. The E_{2g} mode is an in-plane Boron mode while the B_{1g} mode is an out-of-plane Boron mode. Note the degenerate in-plane modes have higher energy than the out-of-plane mode, consistent with (but not proof of) strong in-plane covalent Boron bonds. The two lower energies modes E_{1u} and A_{2u} are collective in-plane and out-of-plane motions of the Zr/Hf and both Boron atoms of the unit cell. Experimental determination of the vibrational spectra of these materials is not currently available.

From the phonon spectra, basic thermodynamic functions can be calculated within the quasiharmonic approximation to the Helmholtz free energy

$$F_{\text{harm}} = k_B T \sum_n \ln(2\sinh(\hbar\omega_n/2k_B T)). \quad (4)$$

From this, the specific heat of ZrB_2 and HfB_2 as a function of temperature was calculated and is shown in Fig. 7. Experimental data for the ZrB_2 specific heat is available.[24] Agreement between computed and experimental quantities is very good.

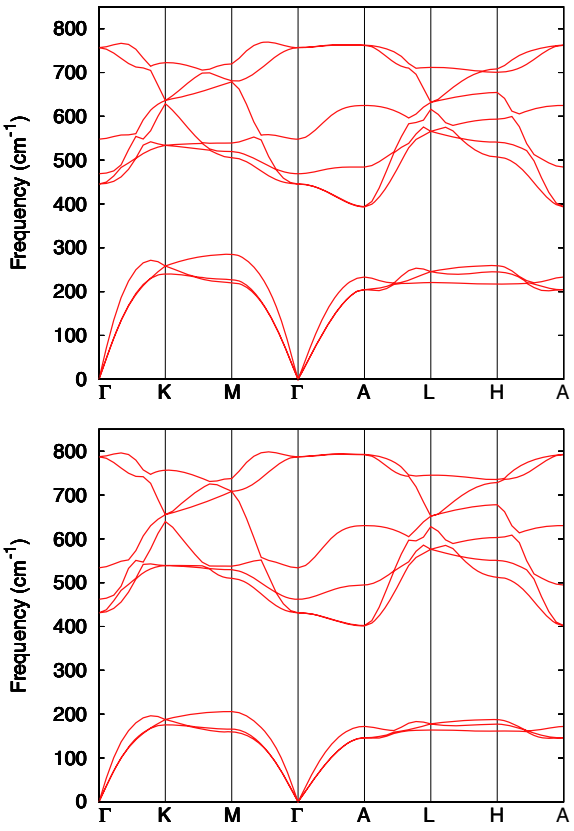

Fig. 6. ZrB_2 (top) and HfB_2 (bottom) phonon dispersions. Acoustic modes are suppressed in HfB_2 relative to ZrB_2 due to Zr/Hf mass difference.

VII. Defects

Finally, the structure and energetics of point defects were evaluated. We examined two types of point defects: vacancies and antisite defects. Vacancies are empty sites in the crystal lattice whereas antisite defects arise when the wrong atomic species is assigned to a given lattice site. In our computations, supercells of size 4 × 4 × 4 were considered to reduce the interactions between the defects and their periodic images. Vacancy formation energies were calculated as

$$E_{vac} = [E(N-1) + E_{atom}(vac)] - E(N) \quad (5)$$

while antisite formation energies were

$$E_{\text{anti}} = E(N) - [E(\text{sub}) - E_{\text{atom}}(\text{sub}) + E_{\text{atom}}(\text{antisub})]. \quad (6)$$

where $E(N)$ is the total energy for a configuration of N atoms and E_{atom} refers to the energy of an isolated atom. We calculated formation energies both with and without relaxation. Results are presented in Table IV using both the FHI–Tr–Ma and the PAW potentials, both using the PBE functional. Agreement with both potential types is very good. PAW potentials with large cores ($Z = 4$) and small cores ($Z = 12$) gave similar results. Spin polarized calculations showed that the defect configurations are spin singlets.

Vacancy formation energies for the metal vacancies are higher than those for the Boron vacancies by roughly 2.0 eV. For the three vacancies considered (Zr, Hf, and B), relaxation had only a small effect; formation energies were reduced by roughly 0.1–0.2 eV. However, the situation is very different for the antisite defects. Unrelaxed antisite formation energies for Zr/Hf are very similar to that of Boron. Upon relaxation, however, the formation energies were reduced by almost 6.0 eV for the Zr/Hf defects. This is not surprising since the Zr/Hf antisite defect requires a very large metal atom to be inserted into a lattice site normally occupied by a relatively small Boron atom. Relaxation of the considerable strain created in these configuration introduces significant distortion of the bond angles for the neighboring Borons. The left pane of Fig. 8 shows a relaxed configuration for an Zr antisite defect in a Boron plane. Conversely, insertion of a Boron into a normally metallic lattice site causes relatively little disruption as can be seen in the right pane of Fig. 8. This is also reflected in the smaller difference between relaxed and unrelaxed formation energies for the Boron antisites which is roughly 0.1–0.2 eV.

Table III. Γ Point Optical Phonon Frequencies (cm^{-1})

	E_{1u}	A_{2u}	B_{1g}	E_{2g}
ZrB_2				
PBE–Tr–Ma	446	469	548	757
PBE–PAW	455	477	572	773
HfB_2				
PBE–Tr–Ma	431	462	534	787
PBE–PAW	445	467	547	806

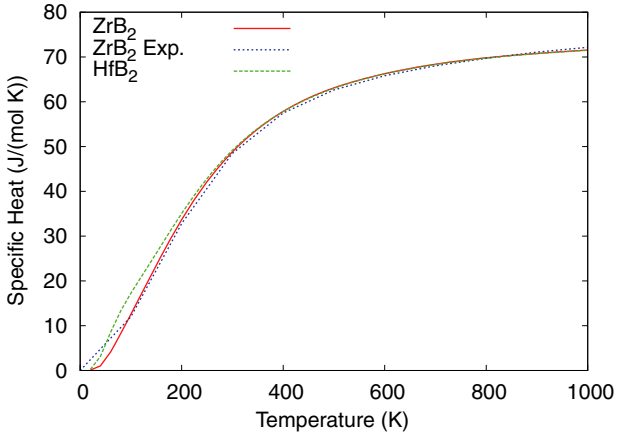

Fig. 7. Lattice contribution to the specific heat for ZrB_2 (solid/red) and HfB_2 (dashed/green) versus temperature in the quasi-harmonic approximation. Agreement between computed and experimental values is excellent.

Table IV. Point Defect Formation Energies (eV). Quantities in Parenthesis are Unrelaxed

	TM Vac	B Vac	TM Antisite	B AntiSite
ZrB_2				
PBE–Tr–Ma	11.20(11.38)	9.33(9.57)	11.22(16.84)	8.58(8.75)
PBE–PAW	11.58(11.74)	9.36(9.59)	11.15(17.45)	8.84(9.01)
HfB_2				
PBE–Tr–Ma	10.60(10.84)	9.00(9.23)	11.61(17.44)	8.40(8.58)
PBE–PAW	11.21(11.33)	9.09(9.24)	11.44(17.46)	8.99(9.08)

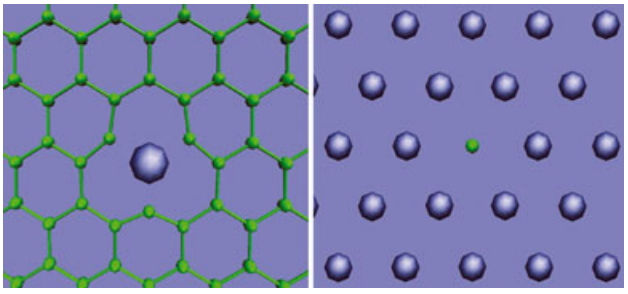

Fig. 8. Relaxed configurations for Zr (left) and B (right) antisite defects. The Zr antisite has significantly more lattice distortion (bond lengths and bond angles) than does the B antisite and a corre spondingly higher formation energy.

VIII. Conclusion

In this article, we performed a comprehensive *ab initio* analysis of the materials ZrB_2 and HfB_2. These UHTC are characterized by good mechanical properties, high thermal conductivity, and good oxidation resistance. Computations based on DFT were performed to obtain many of the fundamental single crystal properties of these materials. Lattice constants, crystallographic structure, and the full set of elastic constants were found. Examination of the electron density distribution, the electron localization function, and the atomic Bader charges enabled elucidation of the various bonding motifs. Interestingly, all three major bonding patterns exist in these materials: covalent bonding in the Boron planes, metallic bonding in the Zr/Hf planes and ionic bonding between the planes. Electronic structure computations identify these materials as semi-metals with the Fermi level positioned in the DOS between full bonding states, and empty, antibonding states. This pseudogap is in part responsible for the favorable mechanical properties of these materials. However, a finite DOS at the Fermi level results in metallic behavior of these materials, including high thermal conductivity. Because of the isoelectronic nature of Zr and Hf and also their comparable atomic radii, many properties of these materials are similar. Lattice dynamical properties, however, are different, owing to the nontrivial mass difference between Zr and Hf. This affects most strongly the acoustic phonon modes. Finally, we computed the structures and formation energies for various point defects. Here, the size difference between Zr/Hf and B play a significant role especially for the antisite defects. Large distortions are seen for the metal antisites (inserting a large metal atom into a B lattice site) whereas B antisites are much less disruptive.

Acknowledgments

J.W.L. and C.W.B are civil servants in the Entry Systems and Technology Division. M.S.D was supported under a NASA prime contract to ELORET Corporation.

References

[1]L. Kaufman and E.V. Clougherty, Investigation of Boride Compounds for Very High Temperature Applications, RTD-TRD-N63-4096, Part III. ManLabs Inc., Cambridge, MA, 1966.

[2]M. J. Gasch, D. T. Ellerby, and S. M. Johnson, "Ultra High Temperature Ceramic Composites"; pp. 197–224 in Handbook of Ceramic Composites. Edited by N. P. Bansal. Kluwer Academic, Boston, 2005.

[3]R. Loehman, E. Corral, H. P. Dumm, P. Kotula, and R. Tandon, Ultra High Temperature Ceramics for Hypersonic Vehicle Applications. SAND2006-2925, Albuquerque, NM, 2006.

[4]W. G. Fahrenholtz, G. E. Hilmas, I. G. Talmy, and J. A. Zaykoski, "Refractory Diborides of Zirconium and Hafnium," *J. Am. Ceram. Soc.*, **90**, 1347–64 (2007).

[5]W. G. Fahrenholtz, G. E. Hilmas, S. C. Zhang, and S. Zhu, "Pressureless Sintering of Zirconium Diboride: Particle Size and Additive Effects," *J. Am. Ceram. Soc.*, **91**, 1398–404 (2008).

[6]J. Perdew, K. Burke, and M. Ernzerhof, "Generalized Gradient Approximation Made Simple," *Phys. Rev. Lett.*, **77**, 3865–8 (1996).

[7]G. Kresse and J. Furthmller, "Efficiency of Ab-Initio Total Energy Calculations for Metals and Semiconductors Using a Plane-Wave Basis Set," *Comput. Mat. Sci.*, **6**, 15–50 (1996).

[8]G. Kresse, and J. Furthmller, "Efficient Iterative Schemes for Ab Initio Total-Energy Calculations Using a Plane-Wave Basis Set," *Phys. Rev.*, **54**, 11169–86 (1996).

[9]G. Kresse, and D. Joubert, "From Ultrasoft Pseudopotentials to the Projector Augmented-Wave Method," *Phys. Rev.*, **59**, 1758–75 (1999).

[10]X. Gonze, G.-M. Rignanese, M. Verstraete, J.-M. Beuken, Y. Pouillon, R. Caracas, F. Jollet, M. Torrent, G. Zerah, M. Mikami, Ph. Ghosez, M. Veithen, J.-Y. Raty, V. Olevano, F. Bruneval, L. Reining, R. Godby, G. Onida, D. R. Hamann, and D. C. Allan, "A Brief Introduction to the ABINIT Software Package," *Zeit. Kristallogr.*, **220**, 558–62 (2005).

[11]X. Gonze, B. Amadon, P.-M. Anglade, J.-M. Beuken, F. Bottin, P. Boulanger, F. Bruneval, D. Caliste, R. Caracas, M. Cote, T. Deutsch, L. Genovese, Ph. Ghosez, M. Giantomassi, S. Goedecker, D. R. Hamann, P. Hermet, F. Jollet, G. Jomard, S. Leroux, M. Mancini, S. Mazevet, M. J. T. Oliveira, G. Onida, Y. Pouillon, T. Rangel, G.-M. Rignanese, D. Sangalli, R. Shaltaf, M. Torrent, M. J. Verstraete, and G. Zerah, J. W. Zwanziger, "ABINIT: First-Principles Approach of Materials and Nanosystem Properties," *Comput. Phys. Commun.*, **180**, 2582–615 (2009).

[12]M. Fuchs and M. Scheffler, "Ab Initio Pseudopotentials for Electronic Structure Calculations of Poly-Atomic Systems Using Density-Functional Theory," *Comput. Phys. Commun.*, **119**, 67–98 (1999).

[13]A. D. Becke and K. E. Edgecombe, "A simple Measure of Electron Localization in Atomic and Molecular Systems," *J. Chem. Phys.*, **92**, 5397–403 (1990).

[14]A. Savin, O. Jepsen, J. Flad, O. K. Andersen, H. Preuss, and H. G. von Schnering, "Electron Localization in Solid-State Structures of the Elements â€" Structures of the Elements - the Diamond Structure," *Angewandte Chemie-International Edition in English*, **31**, 187–8 (1992).

[15]G. Henkelman, A. Arnaldsson, and H. Jonsson, "A Fast and Robust Algorithm for Bader Decomposition of Charge Density," *Comp. Mat. Sci.*, **36**, 354–60 (2006).

[16]P. Vajeeston, P. Ravindran, C. Ravi, and R. Askamani, "Electronic Structure, Bonding, and Ground-State Properties of AlB2-Type Transition-Metal Diborides," *Phys. Rev. B*, **63**, 045115–27 (2001).

[17]H. Ihara, M. Hirabayashi, and H. Nakagawa, "Band Structure and X-Ray Photoelectron Spectrum of ZrB2," *Phys. Rev. B*, **16**, 726–30 (1977).

[18]C. S. Lue and W. J. Lai, "NMR Study of B-2p Fermi-Level Density of States in the Transition Metal Diborides," *Phys. Stat. Sol.(b)*, **5**, 1108–2 (2005).

[19]N. L. Okamoto, M. Kusakari, K. Tanaka, H. Inui, and M. Yamaguchi, "Temperature Dependence of Thermal Expansion and Elastic Constants of Single Crystals of ZrB2 and the Suitability of ZrB2 as a Substrate for GaN Film," *J. App. Phys.*, **93**, 88–94 (2003).

[20]S. T. Mahmud, A. K. M. A. Islam, and F. N. Islam, "VB2 and ZrB2: a Density Functional Study," *J. Phys. Condens. Matter*, **16**, 2335–46 (2004).

[21]I. R. Shein and A. L. Ivanovskii, "Elastic Properties of Mono- and Polycrystalline Hexagonal AlB2-Like Diborides of s, p and d Metals from First-Principles Calculations," *J. Phys. Condens. Matter*, **20**, 415218–28 (2008).

[22]D. R. Hamann, X. Wu, K. M. Rabe, and D. Vanderbilt, "Metric Tensor Formulation of Strain in Density-Functional Perturbation Theory," *Phys. Rev.*, **71** 035117–30 (2005).

[23]C. Lee and X. Gonze, "Ab-Initio Calculation of the Thermodynamic Properties and Atomic Temperature Factors of SiO_2 Alpha-Quartz and Stishovite," *Phys. Rev.*, **51**, 8610–3 (1995).

[24]M. W. Chase, NIST-JANAF Thermochemical Tables, 4th edition, American Institute of Physics, Woodbury, NY, 1998. □